THE ASTROPHYSICAL JOURNAL, 488:224–233, 1997 October 10

ALL-SKY 4.85 GHz FLUX MEASUREMENTS OF H II REGIONS

THOMAS A. KUCHAR[1] AND FRANK O. CLARK
Phillips Laboratory, Optical Environment Division, Backgrounds Branch (GPOB), 29 Randolph Road, Hanscom AFB, MA 01731-3010
Received 1997 March 14; accepted 1997 May 27

ABSTRACT

We present an all-sky flux catalog of 760 H II regions with angular sizes ranging up to 10′ at 4.85 GHz. The data were compiled in a self-consistent manner from existing images of the Green Bank and Parkes-MIT-NRAO 4.85 GHz radio continuum surveys. Nearly 35% of these H II regions have fluxes measured from these surveys for the first time. We compared our results to the previously published source catalogs that fit the same data. The new flux measurements agree within 5%–7% of these values and fall well within the formal errors. The diameters fall within 16% of the previously published fits to the same data, which is within the formal uncertainties of these values.

Subject headings: catalogs — H II regions — radio continuum: ISM — surveys

1. INTRODUCTION

Large-scale astronomical surveys provide a wealth of information for a large number of sources in a single, comprehensive, and self-consistent database. In particular, data from radio continuum surveys can be used for statistical analysis of models as well as for correlations with other survey data. Fluxes and sizes for H II regions over the entire sky were derived at a single frequency using published radio continuum surveys. The intent of this all-sky survey is to provide a database of extended H II regions from which we may extract infrared fluxes. We present here our catalog of 4.85 GHz radio fluxes and diameters for these H II regions.

Nearly 92% of the sky has been surveyed at 4.85 GHz by groups from the Australia Telescope National Facility[2] (ATNF), the Massachusetts Institute of Technology (MIT), and the National Radio Astronomy Observatory[3] (NRAO). Maps of the northern hemisphere ($0° < \delta < 75°$) used data from the NRAO 91 m telescope (Condon, Broderick, & Seielstad 1989; hereafter the 87GB survey). The southern hemisphere ($-87° < \delta < +10°$) maps were constructed from data from the ATNF 64 m Parkes telescope (Condon, Griffith, & Wright 1993; Tasker et al. 1994; Tasker et al. 1997; hereafter the PMN [Parkes-MIT-NRAO] surveys). From these surveys, several source catalogs have been compiled using various methods of source detection and parameterization. Northern hemisphere catalogs were compiled most notably by Gregory & Condon (1991; hereafter the 87GB source catalog) and Becker, White, & Edwards (1991). The southern hemisphere source data encompass several papers by the PMN group (Griffith & Wright 1993; Wright et al. 1994; Griffith et al. 1994; Griffith et al. 1995; Wright et al. 1996; hereafter the PMN source catalogs) as well as a catalog by Gregory et al. (1994) using the same source-detection methods as the 87GB catalog.

We required a self-consistent database of fluxes and angular sizes of H II regions over the entire sky, for which we used the 87GB and PMN radio continuum surveys. Although observed with different telescopes, these surveys were conducted in a similar fashion, and both used the same NRAO multibeam receivers. These self-consistent radio surveys of the majority of the northern and southern hemisphere provide an excellent resource for determining H II region fluxes.

We elected to make a new, comprehensive measurement effort including all H II regions observed in both surveys for three reasons: (1) the 87GB catalog data were measured directly from the images, whereas the PMN catalog data were measured from the processed scan data; (2) the 87GB and PMN catalogs used different noise criteria for source detection; and (3) the different source fitting methods used in 87GB and PMN catalogs were optimized for point sources. Our primary interest is extended sources.

In the following sections, we present the methodology used for measuring H II region fluxes and angular sizes (§ 3). The new measurements are compared with the previously published source catalogs that used the same data (§ 4). Since both the 87GB and PMN surveys overlap near the celestial equator, we compare the separate results for this region (§ 5). In the next section, we briefly describe our source list and the 87GB and PMN surveys.

2. SOURCE LISTS AND SURVEYS

All H II regions examined here are listed in previously published works. The sources were identified from either optical or radio recombination line surveys. Table 1 lists each reference, the sky coverage, and the number of H II regions in each catalog. Removal of duplicate sources left a list of 1048 unique, northern- and southern-hemisphere H II regions.

The 87GB catalog contained only 28% of the sources listed in the northern hemisphere. The PMN source catalog fared better, with nearly 59% coverage in its surveyed area. The 87GB catalog excluded most Galactic sources as a result of source confusion, a problem that also plagued this effort. The sensitivity to weak sources was diminished near stronger sources ($\gtrsim$10 Jy) because of the sidelobe response in the 87GB survey. This was a major problem within 5° of the Galactic plane and is responsible for the smaller number of Galactic sources in the 87GB catalog.

[1] Dynamics Research Corporation, 60 Frontage Road, Andover, MA 01810-5498.

[2] The Australia Telescope National Facility is operated in association with the Division of Radiophysics by CSIRO.

[3] The National Radio Astronomy Observatory is operated by Associated Universities, Inc., under contract with the National Science Foundation.

TABLE 1

H II Region References

Reference	Range in ℓ (deg)	Number of Sources
Caswell & Haynes 1987.....	233–360 0–14	317
Downes et al. 1980	357–360 0–60	170
Fich & Blitz 1984.....	6–243	240
Lockman 1989	350–360 0–253	462
Reifenstein et al. 1970	348–360 0–84	120
Wilson et al. 1970	261–360 0–50	149

Table 2 summarizes the parameters of the 87GB and PMN surveys. For each survey, the table lists the declination range of the survey, image resolution, pixel size, and noise levels. The PMN survey was separated into zones for observational ease. A fourth zone, which covered the zenith of the Parkes telescope, was not included in this work. This zone was observed differently than the other three because of mechanical limitations of the Parkes telescope. Maps for this region were in preparation (Tasker et al. 1997) at the time of this analysis; however, a source catalog was recently published (Wright et al. 1996).

The 87GB and PMN surveys were mapped with the NRAO seven-beam receiver, which was built specifically for rapid mapping of the sky at high frequencies. The 91 m Green Bank telescope performed the northern survey in 1987 and the 64 m Parkes telescope observed the equator and southern hemisphere in 1990. Both telescopes scanned the meridian, alternating north and south, as the sky transited the telescope. The beams of the receivers were arranged in a hexagonal pattern to maximize sky coverage. The arrangement of the beams and scan rates were such that the beams traced seven equally spaced tracks on the sky. The centers of each track were approximately separated by the FWHM beam width of the respective telescope (3.′1 × 2.′8 for the NRAO 91 m, 4.′2 for the Parkes 64 m). Nyquist sampling was easily obtained by shifting the starting position of a previously observed scan path by one-half of a beam width.

The processed scan data from each telescope were used to construct 1024 × 1024 pixel images. The 87GB pixel size is 40″, making the images 11.°4 on a side. The PMN pixels are larger at 60″, with images 17.°1 on a side. The 87GB image centers are separated by 10° in both right ascension and declination, and the PMN images are similarly separated by 15°. Thus, adjacent images overlap by $\lesssim 1°$. This allowed multiple measurements of some of the H II regions, which provided consistency checks for the map reconstruction methods used in both surveys as well as our cataloging methods. These measurements also provided another estimate of the flux uncertainties of not only the H II regions with multiple measurements but also those sources present in only a single image.

TABLE 2

Survey Parameters

Survey	δ Coverage (deg)	Resolution (arcmin)	Pixel Size (arcsec)	σ_n (mJy)
87GB	0 to +75	3.7 × 3.3	40	5–8
PMN:				
Southern	−87.5 to −37	4.9	60	5–13
Tropical	−29 to −9.5	5.0	60	9–11
Equatorial.....	−9.5 to +10	5.0	60	9

Examination of column (3) of Table 2 reveals that the image maps do not have the same resolution as the telescopes that observed them. When scan data for both surveys were converted to image data, they were convolved with a Gaussian tapered sinc restoring function that somewhat reduced the resolution of the image data. The resolution of the survey maps listed in Table 2 are the measured FWHM point-source responses determined by the surveys' respective authors.

The rms noise uncertainties vary with declination in both surveys as a result of the meridian scanning method employed in the data collection. The scan tracks flared out in right ascension and overlapped more as the scan tracks approached the pole, which had the benefit of reducing the noise levels and increasing the flux sensitivity in the image data. Column (5) in Table 2 shows the range in rms noise levels for each survey. Although both surveys provide accurate flux uncertainty with declination measurements, we measure the rms uncertainty in every image examined, since strong ($\gtrsim 10$ Jy) sources can produce local noise enhancements in certain images. In some cases, these strong sources can add significant sidelobe response in the data. (This mainly affected images that contained strong sources such as Cas A, Cyg A, and W51.) Also, noise levels are higher than average near solar noon observations ($12^h < \alpha < 20^h$).

In the construction of the 87GB and PMN images, running median baselines were subtracted to correct for variations caused in part by receiver drifts and atmospheric emission. The baselines have a length of 40′ for the 87GB images and 57′ for the PMN images. Two unintended results of removing these baselines are the suppression of extended emission (for sources of 20′–30′ in extent) and reduction of a source's peak flux. To circumvent the first problem, we only considered H II regions with angular sizes under $\sim 10'$. Hence large, extended sources are absent from this catalog. For the second problem, Gregory & Condon (1991) and Gregory et al. (1994) calculated corrections (ΔS) to the peak fluxes (S_p) for the 87GB and PMN surveys, respectively. Both papers also provide analytic corrections to the fluxes:

$$\Delta S(\mathrm{Jy}) \approx 0.0022 + 0.0007 \log [S_p(\mathrm{Jy})] \quad (87\mathrm{GB}) \quad (1a)$$

$$\Delta S(\mathrm{Jy}) \approx 0.0092 + 0.0035 \log [S_p(\mathrm{Jy})] - 0.0054\{\log [S_p(\mathrm{Jy})]\}^2 \quad (\mathrm{PMN})\,. \quad (1b)$$

The fluxes quoted in the final list of H II regions are corrected for the loss of flux from the running baseline subtraction using equations (1a) and (1b). For most sources, these corrections amount to $\Delta S \lesssim 2.5$ mJy for the 87GB data and 10 mJy for the PMN data.

The standard errors (σ_S) associated with the image fluxes depend on noise (σ_n), background confusion with faint sources (σ_c), and an intensity-proportional error, γ:

$$\sigma_S = \sqrt{\sigma_n^2 + \sigma_c^2 + (\gamma S)^2}\,. \quad (2)$$

The ranges of σ_n for both surveys are listed in Table 2 with the noise levels decreasing toward the poles. For peak flux densities, γ was estimated as 0.12 and 0.10 and σ_c as 1 and 2 mJy for the 87GB and PMN surveys by their respective

authors. Since most of the H II regions are fairly strong sources, the standard errors are dominated by the intensity-proportional term of equation (2).

3. MEASUREMENT OF SOURCES

The H II region source catalog produced here was constructed by measuring the fluxes and sizes directly from the FITS images rather than fitting functions to the source brightness distribution. Automated and interactive software was written to estimate the rms noise (σ_n) in the image, to measure the peak and spatially integrated flux above the $5\sigma_n$ noise limit, and to record the number of source pixels above this limit. The estimates for σ_n were measured directly from each image by determining the variations in the background at the image corners. Areas that contained sources were avoided in this calculation.

We were especially interested in measuring the sizes of extended H II regions and developed an automated algorithm for this purpose. This was done by delimiting a rectangular area in which the pixel values at the boundaries dropped below the $5\sigma_n$ noise limit. When the automated program encountered an H II region with reliably detected emission ($S \gtrsim 5\sigma_n$ at the input position), two lines of 40 pixels in length, parallel to the X- and Y-axes of the image and centered on the H II region, were examined. The four positions along these lines where the pixel value dropped below the $5\sigma_n$ limit were noted. If the pixel values did not fall below the $5\sigma_n$ limit, then the position of the local minimum was recorded instead. (This was an indication that another source might be nearby.) The rectangular area determined by these four points defined the size of the H II region.

Individual pixels, S_i, with fluxes above the noise limit were used to calculate the angular size, Θ, of the H II regions as they appear in the images. {The actual H II region diameters are convolved with the Gaussian-shaped point-source response function of the respective survey images [see Table 2, col. (3)] and can be obtained from the measured diameters: $\Theta_{\rm H\,II} = (\Theta^2 - \Theta^2_{\rm psf})^{1/2}$.} Although the H II regions were delimited by a box, most sources appeared circular or elliptical within the box down to the $5\sigma_n$ contour. We used a one-dimensional fit to determine Θ for ease in calculation. Therefore, we assumed that the emission distribution could be described as a circular Gaussian with the FWHM being

$$\Theta = \sqrt{\frac{8 \ln 2}{2\pi} \frac{\sum S_i \Delta\Omega}{S_p}}, \qquad (3)$$

where $\Delta\Omega$ is the solid angle of a pixel and S_p is the peak flux density of the brightest pixel in the box. This one-dimensional approach worked well when compared to the geometric mean of the elliptical Gaussian fits used in the 87GB and PMN source catalogs (see discussion below).

In § 4, we estimate the uncertainty in Θ as $\sim$16%, based on comparisons to the 87GB and PMN source catalogs. In general, the error in measuring Θ depends on uncertainties in the flux values in equation (3), pointing errors, and systematic measuring errors. For bright sources, the intensity-proportional term of the flux uncertainties (eq. [2]) dominates the noise and confusion uncertainties associated with equation (3). Thus, the formal errors of equation (3) amount to $\sim$5% of Θ. The pointing errors vary with sky position and can be as large 20″, which contributes $\sim$5% for most sources. (Condon et al. 1989 and Griffith & Wright 1993 provide explicit formulae for the pointing errors.) Systematic errors associated with the measurement of the source (e.g., only source pixels are included in the rectangular areas) will also add a few percent to the uncertainty in Θ. Although such an error is difficult to quantify explicitly, it is at most equal in magnitude to the flux and pointing uncertainties. For weaker sources ($<$100 mJy), however, the error in Θ is likely to be larger ($\sim$25%), since some of the emission associated with the H II region may not exceed the $5\sigma_n$ threshold (see discussion in § 4).

Automated routines like the one described above work reasonably well for isolated sources but fail in complex fields. However, complex fields manifest themselves in the data in predictable ways: (1) the perimeter of rectangular area does not reach the $5\sigma_n$ flux limit or the relative minimum within the 40 pixel limit resulting in unusually large areas; (2) large differences exist between the position of the peak flux and the input position of the H II region, possibly indentifying another nearby source; and (3) more than one H II region reports the same position for the peak flux. When these types of failures occurred, the H II regions were examined interactively, with the rectangular area set by the user.

After the initial pass through the images, the distribution of input and peak flux positional differences had a break in the distribution at approximately 1.5 beamwidths for each survey. This seemed an obvious cutoff point for reexamination, and those sources with positional differences larger than the 1.5 beamwidth cutoff were measured interactively. Twenty-three H II regions in the 87GB survey and 49 in the PMN surveys had positional differences larger than this cutoff value. Since the peak emission of some of these H II regions appeared to be blended with a stronger source nearby, they were eliminated from the final source list. The resulting mean differences between the recombination line and the peak flux positions were $1\farcm8 \pm 1\farcm4$ and $2\farcm7 \pm 1\farcm9$ for the 87GB and PMN data, respectively ($\sim 3 \pm 2$ pixels for both surveys).

Four pairs of sources in both surveys reported the same peak. In each of these cases, the algorithm identified a weaker source with the peak of a nearby stronger one. The source closer to the peak was retained in the list, while the other was discarded. The weaker sources could not be measured easily using the interactive program.

The images where the most failures occurred were in the first and fourth Galactic quadrants, although a few failures occurred in images of large, spatially extended objects. When source density in the Galactic plane became too high for the automated algorithm to operate efficiently, the images were examined interactively. Some of the H II regions were spaced so closely that either individual peaks could not be resolved or the sources appeared blended and could not be separated. In these cases, the sources were skipped.

The 87GB images contained 267 measurable H II regions and the PMN images had 513. The positions of these H II regions are plotted in Figure 1. Twenty sources appeared in the overlap region of the surveys. The regions outside the surveys as well as the overlap regions are marked in the figure. Tables 3 and 4 contain the final list of H II region flux and size measurements for the 87GB and PMN surveys, respectively. Abbreviated versions of these tables are given here. Both tables are published in their entirety on AAS CD-ROM Series Volume 9 and are also available from the

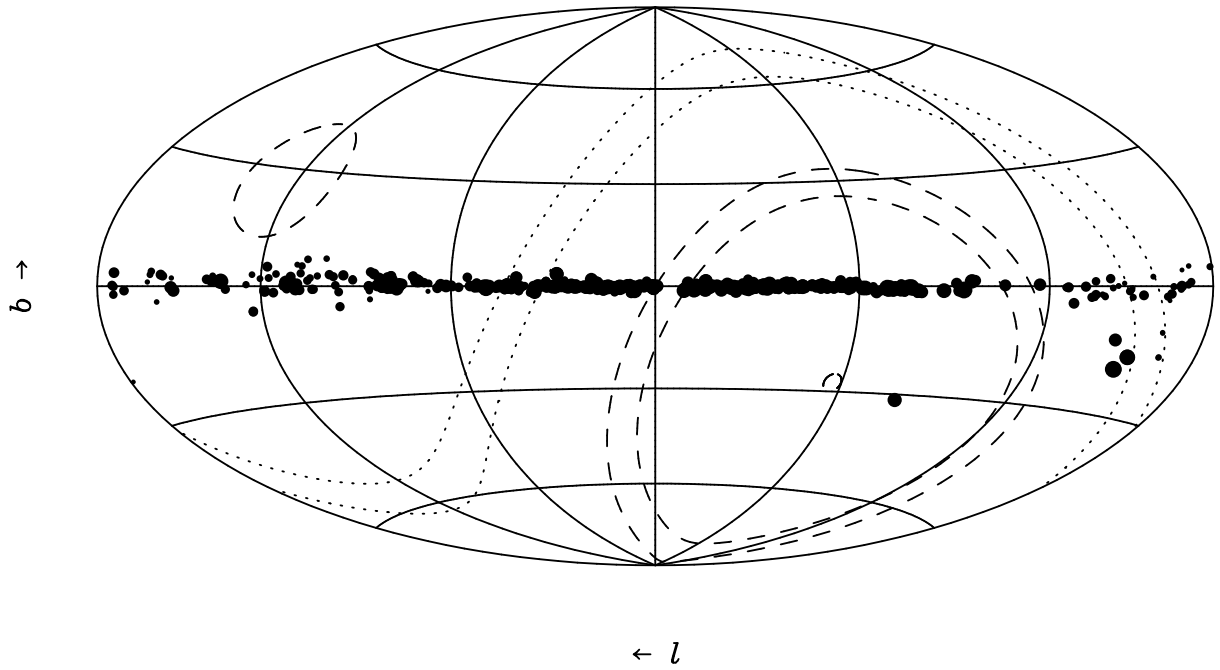

FIG. 1.—An Aitoff projection of the Galaxy with the positions of H II regions in Tables 3 and 4 plotted. The Galactic center is at the center of the figure. Lines of constant longitude are spaced every 60°; lines of constant latitude are spaced every 30°. The size of the point is proportional to the source peak flux, S_p, listed in col. (7) of Tables 3 and 4. Dashed lines mark regions outside of 87GB/PMN survey zones. The region within the dotted lines was covered in both 87GB and PMN surveys.

authors in machine-readable format. Both the printed and electronic versions of the tables have the following format (some aspects of the discussion that follows may not fully apply to the partial tables presented here but apply only to the electronic versions):

Column (1). Source name with the format Glll.l ± bb.b.

Columns (2) and (3). Galactic longitude and latitude (ℓ, b) from references in Table 1.

Column (4). Recombination line velocity, if known, in km s^{-1}.

Columns (5) and (6). Right ascension and declination (α, δ) for epoch 1950.

Column (7). Peak flux density of the H II region in mJy beam^{-1}.

Column (8). FWHM in arcminutes.

Column (9). Reference notes for source position and velocity.

Column (10). Comments (discussed below): A = additional recombination line at this position, T = saturation of the telescope analog-to-digital converters, M = multiple measurement of source, C = complex field, S = stronger source nearby, X = very strong (> 10 Jy) source nearby.

The flux density, S in mJy, of the H II regions can be recovered from the peak flux and angular size:

$$S = S_p(\Theta/\Theta_{\rm psf})^2 , \quad (4)$$

where $\Theta_{\rm psf}$ is the FWHM of the point-source response function (Table 2, col. [3]) of the survey image.

Some of the H II regions in the data tables appear in more than one of the reference catalogs listed in Table 1. The

TABLE 3

87GB SOURCE LIST

Source (1)	ℓ (2)	b (3)	$V_{\rm H\,II}$ (km s^{-1}) (4)	α (1950)[a] (5)	δ (1950)[a] (6)	S_p (mJy beam^{-1}) (7)	Θ[b] (arcmin) (8)	Reference (9)	Comment[c] (10)
G28.8+3.5	28.790	3.486	0.6	18 28 51.5	−2 07 28	12183	7.3	1, 2	
G30.2−0.1	30.227	−0.145	99.4	18 44 24.4	−2 31 43	1436	2.5	1, 2, 3	
G30.3−0.0	30.277	−0.020	97.9	18 44 03.3	−2 25 36	728	4.5	1	S
G30.5+0.0	30.539	0.024	46.1	18 44 22.9	−2 10 25	1327	2.6	1, 3	
G31.0+0.5	31.050	0.480	27.9	18 43 42.2	−1 30 36	1154	4.2	1	
G31.2−0.1a	31.165	−0.127	41.4	18 46 04.3	−1 41 15	1185	3.2	1	
G31.2−0.1b	31.239	−0.108	29.9	18 46 08.4	−1 36 47	1293	4.6	1	
G31.4−0.3	31.401	−0.259	86.2	18 46 58.5	−1 32 19	1486	5.6	1	
G31.6+0.1	31.580	0.101	99.9	18 46 01.5	−1 12 51	353	4.3	1	
G31.6−0.6	31.650	−0.649	80.3	18 48 49.1	−1 29 49	273	4.6	1	

NOTE.—Table 3 is published in its entirety in computer-readable form in the AAS CD-ROM Series, Vol. 9.

[a] Units of right ascension are hours, minutes, and seconds, and units of declination are degrees, arcminutes, and arcseconds.

[b] The actual H II region diameters are convolved with the point-source response function of the respective survey images (see Table 2, col. [3]) and can be obtained from the measured diameters: $\Theta_{\rm H\,II} = (\Theta^2 - \Theta^2_{\rm psf})^{1/2}$.

[c] S = stronger source nearby. See §4 for discussion.

REFERENCES.—(1) Lockman 1989; (2) Reifenstein et al. 1970; (3) Downes et al. 1980.

TABLE 4

PMN Source List

Source (1)	ℓ (2)	b (3)	$V_{H\,II}$ (km s^{-1}) (4)	α (1950)[a] (5)	δ (1950)[a] (6)	S_p (mJy beam^{-1}) (7)	Θ[b] (arcmin) (8)	Reference (9)	Comment[c] (10)
G0.3−0.5.....	0.284	−0.478	20.0	17 44 59.0	−28 55 30	3038	7.4	1	CS
G0.4−0.8.....	0.361	−0.780	20.0	17 46 20.7	−29 00 59	3535	7.2	1	CS
G0.4−0.5.....	0.394	−0.540	24.0	17 45 29.2	−28 51 48	3933	7.5	1	CS
G0.5−0.7.....	0.489	−0.668	17.5	17 46 12.7	−28 50 56	5488	6.2	1	C
G0.5−0.1.....	0.518	−0.065	47.1	17 43 56.0	−28 30 35	22811	6.2	1, 2, 3	SX
G0.6−0.9.....	0.561	−0.850	15.0	17 47 05.6	−28 52 54	2670	6.0	1	S
G0.6−0.6.....	0.572	−0.628	20.0	17 46 15.1	−28 45 26	5703	5.6	1	
G0.7−0.1.....	0.656	−0.058	64.8	17 44 14.1	−28 23 19	42013	6.5	1, 2, 3	TX
G0.8+0.2.....	0.829	0.193	9.7	17 43 40.4	−28 06 35	748	3.4	1	S
G0.9+0.1.....	0.865	0.101	...	17 44 06.9	−28 07 38	5810	4.9	2	

Note.—Table 4 is published in its entirety in computer-readable form in the AAS CD-ROM Series, Vol. 9.

[a] Units of right ascension are hours, minutes, and seconds, and units of declination are degrees, arcminutes, and arcseconds.

[b] The actual H II region diameters are convolved with the point-source response function of the respective survey images (see col. 3, Table 2) and can be obtained from the measured diameters: $\Theta_{H\,II} = (\Theta^2 - \Theta^2_{psf})^{1/2}$.

[c] T = Saturation of the telescope analog-to-digital converters, C = Complex field, S = Stronger source nearby, X = very strong source nearby. See §4 for discussion.

References.—(1) Downes et al. 1980; (2) Reifenstein et al. 1970; (3) Wilson et al. 1970.

same source may have recombination line velocities in these catalogs that vary by a few km s^{-1}. In those cases, the velocities listed in these tables are from the Lockman (1989) catalog. Fich & Blitz (1984) list the CO velocities of molecular clouds that are associated with the optical H II regions rather than a recombination line velocities of the H II regions themselves. Sources that have Fich & Blitz as the only reference list the CO velocities in Tables 3 and 4, which may differ from the recombination line velocity of the H II region by several km s^{-1}. Otherwise, the listed velocities are from the first reference in the list. Also, some surveys have listed two recombination lines at different velocities for the same position. These sources are noted (by A) in column (10) of the data tables.

In both surveys, strong sources saturated the analog-to-digital converters of the data recorders. This occurred at approximately 70 and 40 Jy for the 87GB and PMN surveys, respectively. However, some of the peak fluxes measured from the PMN images exceeded this value. Although these sources are included in Table 4, they are flagged (by T) in column (10) of the table.

Since the image sides overlap by $\sim 1°$, several sources appear in two to four images. The 87GB survey had 51 sources in multiple images and the PMN survey had 99. Averages of the fluxes and diameters for these sources appear in the data tables and are so noted (by M) in column (10).

The sources in complex fields (most of which had to be measured interactively) are denoted by C in column (10). A source was defined to be in a complex field if there were two or more sources within either $2 \times \Theta$ (i.e., four source radii) or $2 \times \Theta_{psf}$, whichever was larger. This examination radius was chosen since it represents $\sim 5\,\sigma$ of the Gaussian brightness distribution. Also, the fluxes of all the sources (from our H II region list as well as both the 87GB and PMN source catalogs) within this radius were examined for strong sources. If a source within the radius defined above has a flux greater than 1.5 times that of the H II region, then an S appears in column (10). This is noted in the tables regardless of the source being in a complex field. If any of these sources is stronger than 10 Jy, another warning flag (X) is also placed in column (10). It is possible that a strong source or its response in the sidelobes might affect the flux and diameter measurements of the H II region.

The set of repeat measurements provided a consistency check for the map reconstruction techniques as well as a second estimate of the uncertainties associated with the fluxes and diameters. In general, stronger sources ($S_p \gtrsim 500$ mJy) showed less relative variation in flux ($\sim$1–2%) than weaker ones ($\sim$4–5%). The flux variations for most of sources were less than the rms noise limit ($5\sigma_n$), indicating that noise was the probable cause for most of the differences. For the remainder of the sources (20 sources for the 87GB data, 40 for the PMN), there are two possible causes for the variations: (1) differences in the gridding of the data caused the variations in the flux measurements and (2) the repeat measurements occur at the edges of the images where projection effects may cause similarly sized boxes to cover different solid angles for the same source.

Most of the source diameters varied between 3% and 6%, although a few had larger variations (10%–20%). There appears to be no direct correlation between the source flux and variations in the diameter. Sources in all flux ranges showed both large and small variations in diameter. Also, relative (i.e., percentage) variations in the source flux seem to be uncorrelated with the variations in diameter.

The data from the multiple measurements for most of the H II regions indicate that the variations are of order the formal uncertainties of the measured quantities in the data tables. This is an indication of the strong consistency of the image-construction techniques as well as measurement algorithms.

4. COMPARISON WITH 87GB AND PMN SOURCE CATALOGS

We compared the on-line versions of the 87GB and PMN source catalogs with the data tables to check the consistency of the newly measured fluxes and diameters with the previously published works that used the same data. The 87GB source catalog contained 102 sources in common with Table 3 and the PMN catalogs had 398 sources in common with Table 4. Figure 2 shows flux-flux plots of these data. Along with the peak fluxes, a reference line of slope unity is plotted. Linear fits of the form log

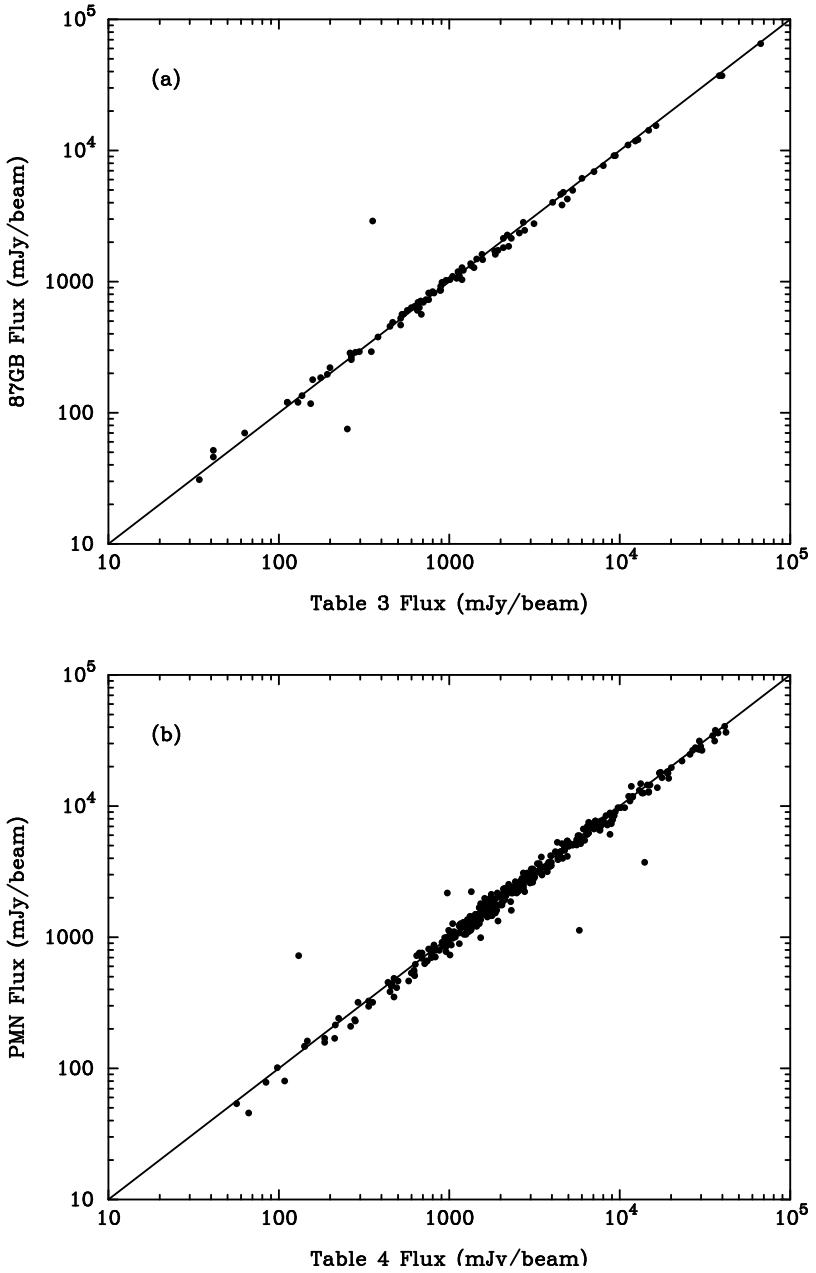

FIG. 2.—Comparison of 4.85 GHz fluxes of H II regions measured for this paper with the previously published source catalogs. The solid line is provided as a reference and has a slope of +1. See Table 1 for the list of catalog references. (*a*) Fluxes from Table 3, col. (7) compared with fluxes from the 87GB source catalog. (*b*) Fluxes from Table 4, col. (7) compared with fluxes from the PMN source catalogs.

$(Y) = A + B \log (X)$ were made to these data. The fits were made as a way to gauge how closely the two independent measurements matched and should not be used as a way to transform between the flux scales, as linear fits of logarithmic quantities tend to give preferential weight to the data with larger values. The slopes of the fitted lines are near unity (see Table 5 and the discussion below), within the uncertainties of the data, which indicates that the fluxes derived from the images are comparable to those of the source catalogs.

The mean of the flux ratios (defined from the plot axes as X/Y) was calculated for the data displayed in Figure 2. On average, the peak fluxes in Tables 3 and 4 are higher than those in the 87GB and PMN source catalogs by 3% and 5%, respectively. The differences are likely the result of fitting a brightness distribution function to the source versus reading the fluxes directly from the images. These results, along with the results of the linear fits, are summarized in the first two entries of Table 5. The table lists the data sets, the coefficients of the fits, the means and standard deviations of the flux ratios, and the numbers of H II regions in the data sets.

To give a better indication of how closely our methods duplicate the results of the fitting procedures employed in the 87GB and PMN source catalogs, we calculated mean error ratios as follows. Both the 87GB and PMN source catalogs quote formal errors for fits to the peak fluxes. The flux error ratio is defined as the flux difference of our result with the previously published one [i.e., $(X - Y)$ following the convention used in the flux ratios above] divided by the published formal error. For the 87GB data, the mean error ratio is 12% $\pm$ 65%, which indicates that most of our fluxes

TABLE 5

LINEAR FITS TO FLUX-FLUX PLOTS: LOG (Y) = A + B LOG (X)

Data Set	A	B	$\langle X/Y \rangle$	N
87GB vs. Table 3.....	0.04	0.98	1.07 ± 0.35	102
PMN vs Table 4	0.03	0.99	1.05 ± 0.27	398
PMN vs 87GB:				
All.....	0.14	0.94	0.99 ± 0.24	3423
$\|b\| < 10°$	0.19	0.93	0.94 ± 0.24	310
Table 3 vs. Table 4.....	0.18	0.93	1.04 ± 0.19	20

are well within the error range of the fitted 87GB fluxes. For the PMN data, the mean error ratio did not fare as well: 65% $\pm$ 190%. Although this ratio is much larger than the 87GB result, it still places 70% of our fluxes within one or two formal errors of the fitted values. A possible reason for this discrepancy is that both the Table 3 and 87GB catalog fluxes were measured directly from the images. The PMN catalog fluxes were measured from the telescope scan data, whereas the Table 4 measurements were taken from image data.

Both the 87GB and PMN source catalogs list the results of elliptical Gaussian fits to the sources. To compare these fitted values with our circular Gaussian FWHM estimates (eq. [2]), we calculated the geometric mean of the major and minor (FWHM) axes in the source catalogs. Figure 3 shows the diameter-diameter comparison of these data. The diameters of the 87GB catalog could be compared directly with the Table 3 data, since both data sets have the same resolution. A diameter ratio was defined in a similar way to the flux ratio above. On average, the Table 3 diameters are 2% larger than those in the 87GB source catalog but, as can be seen in Figure 3*a*, there is a large scatter (1 σ = 16%) in the data. Since the PMN source catalogs have different resolutions from the Table 4 data, the Table 4 data were rescaled to the PMN catalog resolution before being plotted in Figure 3*b*. As a result, 50 H II regions in Table 4 with diameters smaller than the image resolution ($\sim 5'$) were removed from consideration before the data were rescaled. The PMN source catalog diameters are larger on average by 2% than those in Table 4, but again there is a large

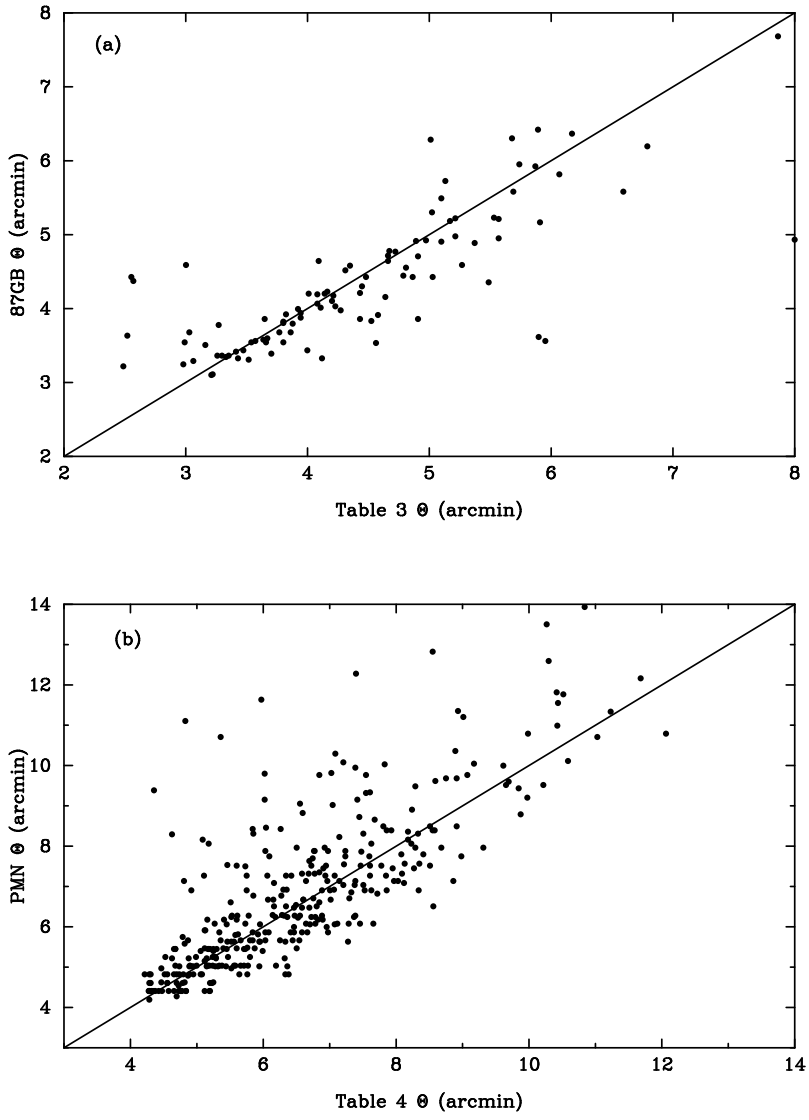

FIG. 3.—Comparison of 4.85 GHz diameters of H II regions measured for this paper with the previously published source catalogs. The solid line is provided only as a reference and has a slope of +1. See Table 1 for the list of catalog references. (*a*) Diameters from Table 3, col. (8) compared with diameters from the 87GB source catalog. (*b*) Diameters from Table 4, col. (8) compared with diameters from the PMN source catalogs. Note that Table 4 measurements were rescaled to the PMN catalog resolution before plotting. See discussion in § 4.

scatter (16%) about the mean. Since this 1 σ scatter is the same for both data sets, 16% represents a reasonable uncertainty in the size measurement.

For the weaker sources ($\lesssim$100 mJy), Θ might be underestimated if some of the flux associated with the source did not exceed the $5\sigma_n$ limit. Therefore, we compared our measurements of Θ for sources with fluxes under 100 mJy with those in the 87GB and PMN source catalogs. Since these catalogs performed Gaussian fits down to a lower baseline noise level, they might provide a more accurate size estimate for the weaker sources. Unfortunately, there were very few (seven) sources in this flux range in common with the 87GB catalog and none in the PMN catalog. However, all of the 87GB sources were larger than those of Table 3, on average, by 25%. When the flux range of the sources was increased, the differences approached the above results. Therefore the uncertainty for weak sources should be regarded as 25% rather than the 16% suggested above.

We compared the differences between the diameters of the source catalogs and our data set with the formal errors computed for the source catalogs. As was done for the fluxes above, a diameter error ratio was similarly defined. The mean ratios were 37% $\pm$ 186% and -29% $\pm$ 137% for the 87GB and PMN data, respectively. The negative sign for the PMN error ratio indicates that the PMN catalog diameters are on average larger than those in Table 4. These results indicate that most of our diameter measurements fall within the uncertainty of the fitted values. Given that three different methods were employed to determine source diameters, our method produced results that are consistent with the disparate fitting methods of the 87GB and PMN source catalogs.

5. SUMMARY AND CONCLUSIONS

The 4.85 GHz fluxes and diameters of the 760 H II regions, which are presented in Tables 3 and 4, provide the most comprehensive list of self-consistent measurements to date. Although the fluxes are slightly brighter than those of the 87GB and PMN catalogs, most of the fluxes measured here fall well within the formal errors of those catalogs. The diameter measurements are on average slightly different from the source catalog measurements, but most fall within the formal uncertainties of the previously published values. These differences are small and can be understood in the context of the different procedures used to obtain the fluxes and diameters.

Although the 87GB and PMN surveys were conducted in a similar manner, they do have differences in sensitivity and resolution. We endeavored to make a consistent analysis of the surveys. However, the differences in flux and size need to be quantified if Tables 3 and 4 are to be used as a single data set. The overlap of the two surveys between $0° < \delta < 10°$ provided a region for comparison of the derived H II regions fluxes and sizes. Griffith et al. (1995) compared the 87GB and PMN source catalogs in this region and found that on average the fluxes agreed to within 2%, with the PMN fluxes being brighter. For the weakest sources, the agreement was within 3%. They concluded that some of the discrepancy may be due to differences in flux-bias corrections, resolution, data reduction techniques, or even source variability from the two different observing epochs of both surveys.

However, Griffith et al. (1995) excluded sources in the Galactic plane ($|b| < 10°$) from their comparison, where most of our sources are located. (Griffith et al. 1995 also excluded the zone between $12^h < \alpha < 20^h$ because of solar contamination in both of the source catalogs. For consistency with their analysis, this region has been excluded in our comparison.) Because of high confusion levels, much of the Galactic plane was excluded from the 87GB source catalog. Unfortunately, our effort suffered from the same high confusion levels in the first and fourth quadrants. As a result, Tables 3 and 4 share only 20 H II regions in common. These few sources and their limited flux range do not provide enough data for an adequate comparison if only our results are used. Since the flux comparisons in § 4 and Figure 2 show a good match between our results and the previously published source catalogs, we compared all the sources common to the 87GB and PMN source catalogs without excluding the Galactic plane. There are 3423 sources in common with the 87GB and PMN source catalogs, 310 in the range $|b| < 10°$. The difference in fluxes between the two source catalogs is slightly more than 1%. For the sample restricted to the Galactic plane, the PMN fluxes are on average 6% brighter than the 87GB fluxes. The discrepancy in the flux differences between these two samples may be due to the complex nature of Galactic plane emission and the effect it has on the median baseline removal for the two surveys.

Figure 4 shows flux-flux plots for the overlap region of the 87GB and PMN source catalogs. For completeness, the data of Tables 3 and 4 are also plotted. Linear fits along with the mean flux ratios were calculated for these data and are summarized in the last three entries of Table 5. It is important to note that the fluxes in Table 3 are on average 4% brighter than those in Table 4. Given the above results along with the flux comparisons in § 4, we had expected the Table 3 fluxes to be only 1% brighter on average. However, there are too few sources to make an adequate comparison.

The linear fits of the two data sets confined to the Galactic plane are nearly identical. Again, this is probably the result of the image fluxes being comparable in value to the source catalog fluxes. However, there are too few sources plotted in Figure 4*b* to make this the sole basis for this conclusion. The results shown in Figure 2 support this conclusion more strongly.

The diameters of the sources in the two source catalogs were compared in the same manner as the fluxes above. However, the resolution differences between the 87GB and PMN data needed to be considered, and the contribution of the respective telescope beams was removed before the data were plotted. Figure 5 shows the diameter comparison for the 87GB and PMN source catalogs and the data set presented in Tables 3 and 4. Again, only sources appearing larger than the beam are plotted in Figure 5. Many of the PMN sources plotted in Figure 4*a* appear pointlike and do not have any corresponding diameter measurements. Therefore, only 254 sources are plotted in Figure 5*a*. Only one of the sources in Tables 3 and 4 appeared smaller than the respective image resolution and therefore was not plotted in Figure 5.

The PMN catalog diameters in Figure 5*a* are on average 25% larger than their corresponding 87GB entries. Most of the Figure 5*a* data are slightly larger than point sources, which causes the beam removal to artificially increase the rms scatter about the mean. However, much of the scatter is intrinsic to the data. The sources in Figure 5*a* are clustered in a region bounded by 1′ to 3′. The H II regions plotted in

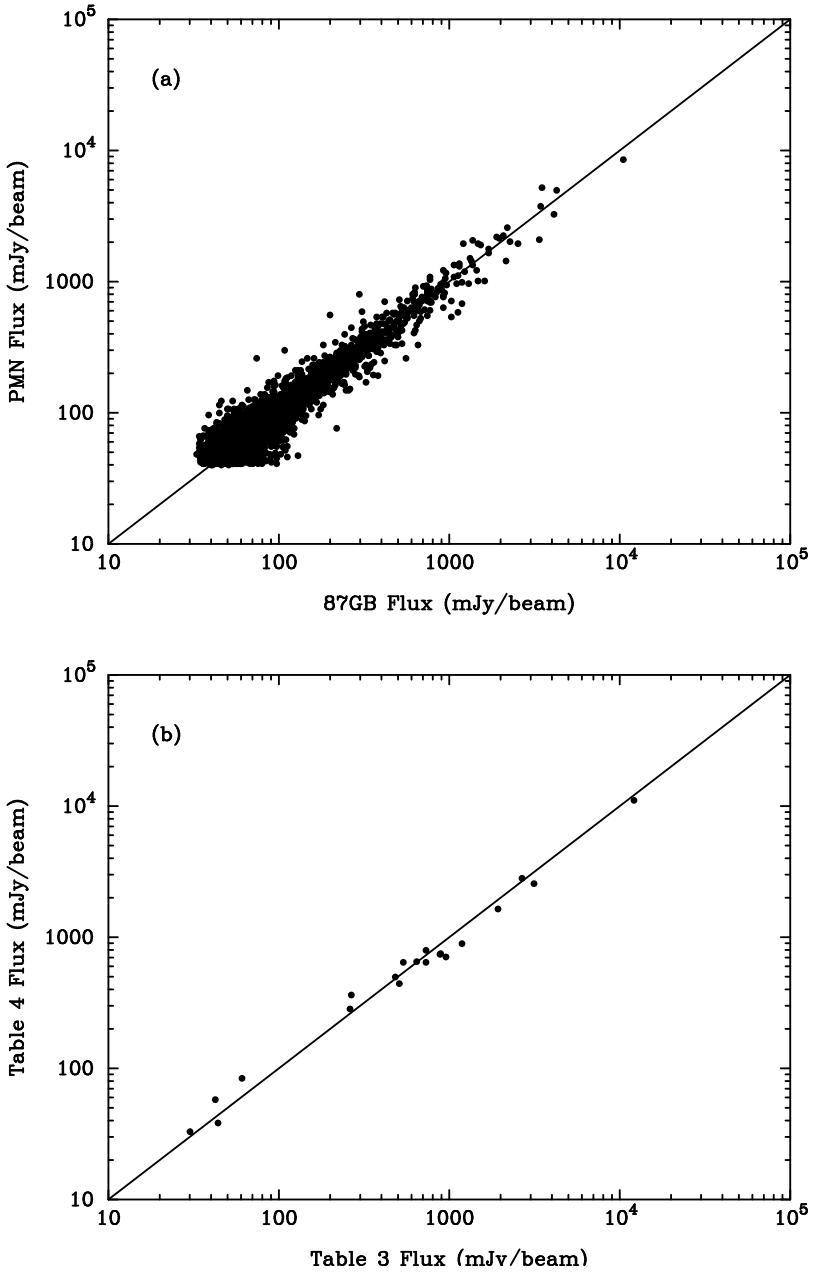

FIG. 4.—Comparison of 4.85 GHz fluxes of sources common to both the 87GB and PMN surveys. The solid line is provided only as a reference and has a slope of +1. (*a*) Fluxes from all sources in the 87GB and PMN source catalogs excluding the region: $12^h < \alpha < 20^h$. See Table 1 for the list of catalog references. (*b*) Fluxes of H II regions from col. (7) of Tables 3 and 4.

Figure 5*b* lie almost exclusively outside this range because the fitting procedures for both the 87GB and PMN source catalogs were optimized for point sources. Unfortunately, there is not a sufficient number of extended sources in the overlap region of either the 87GB or PMN source catalog to determine an adequate relation between the two sets of diameters. Although the sources in Figure 5*b* seem to cluster around the reference line, there are too few sources in Tables 3 and 4 to make a statistically significant correlation between the data sets.

From the comparisons between the two surveys, the fluxes listed in Tables 3 and 4 form a consistent set of measurements. The sources measured in both the 87GB and PMN source catalogs agree within 1%–6%, depending on whether the subset of the data is restricted to the Galactic plane. Thus the flux scales in Tables 3 and 4 should be in agreement to within 6% on average. However, such a statement of comparison cannot be made about the diameters listed in the data tables, since there were too few sources in common to make an adequate analysis. The 87GB and PMN source catalogs preferentially examined point sources. Since a majority of the sources in Tables 3 and 4 are extended, the source catalogs do not provide an appropriate cross section of sources for a comparison of extended objects.

We are grateful to N. Tasker for supplying the PMN survey data. We also acknowledge the number of useful comments made by the referee. Tables 3 and 4 are available in a machine-readable format from the authors.

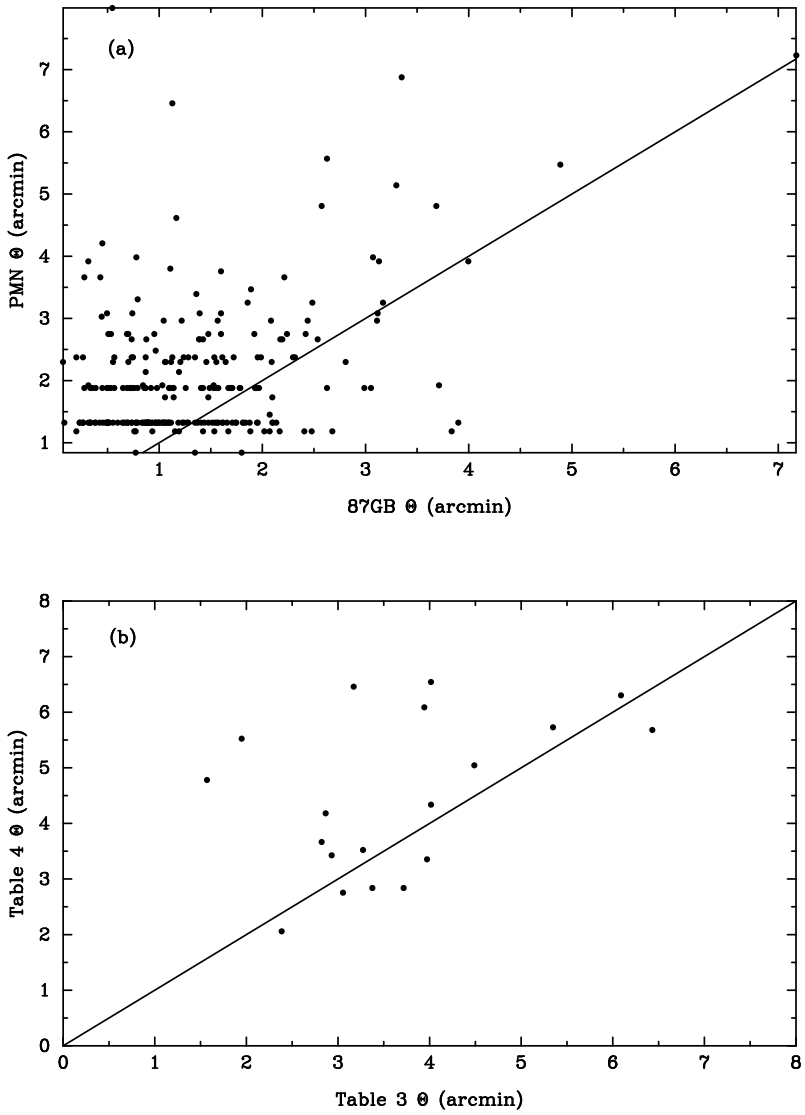

FIG. 5.—Comparison the 4.85 GHz diameters of sources common to both the 87GB and PMN surveys. The solid line is provided only as a reference and has a slope of +1. Note that the effective contribution of the telescope beam has been removed from all data before being plotted. See discussion in § 5. (*a*) Diameters from all sources in the 87GB and PMN source catalogs excluding the region: $12^h < \alpha < 20^h$. See Table 1 for the list of catalog references. (*b*) Diameters of H II regions from col. (8) of Tables 3 and 4.

REFERENCES

Becker, R. H., White, R. L., & Edwards, A. L. 1991, ApJS, 75, 1
Caswell, J. L., & Haynes, R. F. 1987, A&A, 171, 261
Condon, J. J., Broderick, J. J., & Seielstad, G. A. 1989, AJ, 97, 1064
Condon, J. J., Griffith, M. R., & Wright, A. E. 1993, AJ, 106, 1095
Downes, D., Wilson, T. L., Bieging, L., & Wink, J. 1980, A&AS, 40, 379
Fich, M., & Blitz, L. 1984, ApJ, 279, 125
Gregory, P. C., & Condon, J. J. 1991, ApJS, 75, 1011
Gregory, P. C., Vavasour, J. D., Scott, W. K., & Condon, J. J. 1994, ApJS, 90, 173
Griffith, M. R., & Wright, A. E. 1993, AJ, 105, 1666
Griffith, M. R., Wright, A. E., Burke, B. F., & Ekers, R. D. 1994, ApJS, 90, 179
———. 1995, ApJS, 97, 347
Lockman, F. J. 1989, ApJS, 71, 469
Reifenstein, E. C., III, Wilson, T. L., Burke, B. F., Mezger, P. G., & Altenhoff, W. J. 1970, A&A, 4, 357
Tasker, N. J., Condon, J. J., Wright, A. E., & Griffith, M. R. 1994, AJ, 107, 2115
Tasker, N. J., Wright, A. E., & Griffith, M. R. 1997, in preparation
Wilson, T. L., Mezger, P. G., Gardner, F. F., & Milne, D. K. 1970, A&A, 6, 364
Wright, A. E., Griffith, M. R., Burke, B. F., & Ekers, R. D. 1994, ApJS, 91, 111
Wright, A. E., Griffith, M. R., Hunt, A. J., Troup, E., Burke, B. F., & Ekers, R. D. 1996, ApJS, 103, 145